Communication

A Multitrace Surface Integral Equation Solver to Simulate Graphene-Based Devices

Ran Zhao, Liang Chen, Ping Li, Jun Hu, and Hakan Bagci

***Abstract*— A multitrace surface integral equation (MT-SIE) solver is proposed to analyze electromagnetic field interactions on composite devices involving magnetized and nonmagnetized graphene sheets. The computation domain is decomposed into two subdomains: an exterior subdomain that represents the unbounded background medium where the device resides in an interior subdomain that represents the dielectric substrate. Resistive Robin transmission conditions (RRTCs) are formulated to describe the infinitesimally thin graphene sheet that partially covers the surface between the two subdomains. On the rest of this surface, traditional Robin transmission conditions (RTCs) are enforced. The electric and magnetic field equations are used as the governing equations in each subdomain. The governing equations of a subdomain are locally coupled to the governing equations of its neighbor using RRTCs and RTCs. The accuracy and the applicability of the proposed MT-SIE solver are demonstrated by various numerical examples.**

***Index Terms*— Graphene-based device, multitrace (MT), resistive boundary condition (RBC), surface integral equation (SIE).**

I. Introduction

Graphene is a 2-D material with remarkable electrical, mechanical, and thermal properties [1]. Its surface conductivity depends on temperature T, chemical potential (Fermi level) μ_c, and particle scattering rate Γ, and therefore it can be dynamically tuned to manipulate electromagnetic fields. This has led to the development of various graphene-based devices such as thin-film transistors [2], gas sensors [3], solar cells [4], and photonic modulators [5]. In addition, a graphene sheet can be biased using a static magnetic field (which makes its conductivity a tensor), increasing its tunability even more. Magnetized graphene has been used in the design of various tunable electromagnetic devices operating in the different bands changing from microwave to terahertz (THz) frequencies. Some examples of these devices are tunable filters [6], phase shifters [7], reconfigurable THz antennas [8], [9], and frequency-selective surfaces [10].

For almost all of the devices listed above, a graphene sheet is located on a dielectric substrate and its thickness is several orders smaller than any other device dimension. To simulate such a device, one can directly discretize the graphene sheet using volumetric elements but this yields a multiscale mesh with a large number of elements [11]. Furthermore, the resulting matrix system is often ill-conditioned [12], [13]. These bottlenecks can be circumvented by replacing the graphene sheet with an infinitesimally thin surface and enforcing resistive boundary conditions (RBCs) on it [14]–[17]. This approach has been incorporated within finite-difference time-domain method [14], [15] and discontinuous Galerkin time-domain scheme [16], [17], and the resulting solvers have been used to simulate various graphene-based devices. Although these differential equation solvers are versatile in handling geometrically complicated devices, they use a volumetric mesh in the whole computation domain and have to use domain truncation techniques (such as absorbing boundary conditions or perfectly matched layers) and consequently become computationally demanding especially when they are used to simulate large-scale problems.

These bottlenecks can be addressed by switching to an integral equation-based formulation. In [18] and [19], electromagnetic field interactions on a graphene sheet are first formulated in the form of a volume integral equation. Then, this equation is “reduced” into surface integral equations (SIEs) under the thin dielectric sheet approximation [20]. In [21] and [22], an equivalent circuit model is obtained for the graphene sheet using an electric field integral equation, then this model is incorporated into the partial element equivalent circuit method [23]. In [24] and [25], a magnetic field integral equation is solved to analyze electromagnetic scattering from graphene disks and strips that reside in an unbounded medium. None of these integral equation-based approaches deal with the case when a graphene sheet is located on a dielectric substrate.

To address this shortcoming, in [26] and [27], RBCs representing the graphene sheet are solved together with the Poggio–Miller–Chang–Harrington–Wu–Tsai integral equation [28] enforced on the surfaces of the dielectric substrate. These two schemes completely avoid volumetric meshes. However, for geometrically complicated devices, the matrix system obtained by discretizing this coupled system of SIEs with the Rao–Wilton–Glisson (RWG) functions [29] becomes ill-conditioned. This degrades the accuracy and the efficiency of the solvers, especially for electrically-large devices.

In recent years, integral-equation domain-decomposition methods that make use of multitrace SIEs (MT-SIEs) and Robin transmission conditions (RTCs) have found widespread use in the electromagnetic simulation of a wide range of structures changing from penetrable objects to large cavities, composite objects, and so on [30]–[34]. These methods decompose the computation domain into subdomains and enforce SIEs on their (internal) surfaces. Then, SIEs of a given subdomain are “coupled” to SIEs of its neighbors via RTCs. This local-coupling approach improves the scalability and robustness of the traditional “single-domain” SIE solvers and is more suitable for solving large-scale problems.

In this work, an MT-SIE solver is proposed to simulate electromagnetic field interactions on graphene-based devices. The graphene sheet that is located on the surface between the unbounded

Manuscript received 7 August 2021; revised 30 January 2022; accepted 3 April 2022. Date of publication 25 April 2022; date of current version 6 October 2022. This work was supported in part by NSFC under Grant 62031010 and Grant 61801002 and in part by King Abdullah University of Science and Technology (KAUST) Office of Sponsored Research (OSR) under Award 2019-CRG8-4056. *(Corresponding author: Liang Chen.)*

Ran Zhao is with the Division of Computer, Electrical, and Mathematical Science and Engineering (CEMSE), King Abdullah University of Science and Technology (KAUST), Thuwal 23955, Saudi Arabia, and also with the Key Laboratory of Intelligent Computing and Signal Processing, Ministry of Education, Anhui University, Hefei 230039, China (e-mail: ran.zhao@kaust.edu.sa).

Liang Chen and Hakan Bagci are with the Division of Computer, Electrical, and Mathematical Science and Engineering, King Abdullah University of Science and Technology (KAUST), Thuwal 23955, Saudi Arabia (e-mail: liang.chen@kaust.edu.sa; hakan.bagci@kaust.edu.sa).

Ping Li is with the Department of Electronic Engineering, Shanghai Jiao Tong University, Shanghai 200240, China, and also with the Shenzhen Institute of Research and Innovation (SIRI), The University of Hong Kong (HKU), Shenzhen 518063, China (e-mail: ping.li@sjtu.edu.cn).

Jun Hu is with the School of Electronic Science and Engineering, University of Electronic Science and Technology of China (UESTC), Chengdu 611731, China (e-mail: hujun@uestc.edu.cn).

Color versions of one or more figures in this communication are available at https://doi.org/10.1109/TAP.2022.3168699.

Digital Object Identifier 10.1109/TAP.2022.3168699

background medium and the dielectric substrate is described by RBCs. Resistive RTCs (RRTCs) are formulated to incorporate these RBCs within the MT-SIE formulation. The computation domain is decomposed into two subdomains: an exterior subdomain that represents the unbounded background medium where the device resides in an interior domain that represents the dielectric substrate. The electric and magnetic field equations are used as the governing equations in each subdomain. These subdomain SIEs are coupled to each other using RRTCs (that represent the graphene) and "traditional" RTCs (that represent the tangential electric and magnetic field continuity). Note that RBCs and corresponding RRTCs can account for both nonmagnetized graphene (with a scalar conductivity) and magnetized graphene (with a tensor anisotropic conductivity). Compared to the differential equation solvers [12]–[17], the proposed MT-SIE solver avoids volumetric meshes and does not require absorbing boundary conditions. Compared to the SIE solvers developed to simulate only graphene sheets [18], [19], [21], [22], [24], [25], the proposed MT-SIE solver accounts for the dielectric substrate. Furthermore, it inherits all advantages of the MT-SIE solvers developed to simulate composite objects [32]–[34]. It yields a matrix system that can be efficiently solved using an iterative solver even for electrically large devices and allows for higher flexibility in mesh generation for multilayered substrates. Also, note that the formulation proposed in this work can easily be extended for simulation of various devices making use of other 2-D materials and to account for generalized sheet transmission conditions (GSTCs) formulated using (anisotropic) polarization susceptibilities [35], [36].

The rest of this communication is organized as follows. In Section II, first, the surface conductivity of the nonmagnetized and magnetized graphene sheets is provided. This is followed by the derivation of RRTCs for the graphene sheet. Then, MT-SIEs underlying the proposed solver are derived, and the matrix system resulting from their RWG-based discretization is provided. Section III provides numerical examples to demonstrate the accuracy and the applicability of the proposed solver. Conclusions are summarized in Section IV.

II. Formulation

In this section, first, RBCs representing magnetized and nonmagnetized graphene sheets are provided. Then, RRTCs pertinent to these RBCs are derived. This is followed by the detailed mathematical description of the MT-SIE solver developed to simulate graphene-based devices. Note that for the sake of brevity in notation, the dependence on space (i.e., location vector $\mathbf{r}$) is omitted for all variables used in this section.

A. RBCs and RRTCs for Graphene Sheets

The graphene sheet is modeled as a zero-thickness surface with conductivity $\overline{\overline{\sigma}}_{\mathrm{g}}$. RBCs on this surface are expressed as [24]

$$\hat{\mathbf{n}}_1 \times (\mathbf{E}_1 - \mathbf{E}_2) = 0 \tag{1}$$

$$\hat{\mathbf{n}}_1 \times (\mathbf{H}_1 - \mathbf{H}_2) = -\frac{1}{2}\overline{\overline{\sigma}}_{\mathrm{g}} \cdot [\hat{\mathbf{n}}_1 \times \hat{\mathbf{n}}_1 \times (\mathbf{E}_1 + \mathbf{E}_2)] \tag{2}$$

where $\{\mathbf{E}_1, \mathbf{H}_1\}$ and $\{\mathbf{E}_2, \mathbf{H}_2\}$ are the electromagnetic fields on the two sides of the graphene surface and $\hat{\mathbf{n}}_1$ is this surface's unit normal vector pointing into side 1.

Assume the graphene sheet is located on the xy-plane and a static magnetic field with flux $\mathbf{B} = \hat{\mathbf{z}}B_0$ "biases" the graphene sheet. In this case, the surface conductivity $\overline{\overline{\sigma}}_{\mathrm{g}}$ is given by Hanson [37]

$$\overline{\overline{\sigma}}_{\mathrm{g}} = \begin{bmatrix} \sigma_{\mathrm{xx}} & -\sigma_{\mathrm{yx}} & 0 \\ \sigma_{\mathrm{yx}} & \sigma_{\mathrm{xx}} & 0 \\ 0 & 0 & 0 \end{bmatrix} \tag{3}$$

where σ_{xx} and σ_{yx} are approximated by a Drude-like models as

$$\sigma_{\mathrm{xx}} = \sigma_0 \frac{1 + j\omega\tau}{(\omega_c\tau)^2 + (1 + j\omega\tau)^2} \tag{4}$$

$$\sigma_{\mathrm{yx}} = \sigma_0 \frac{\omega_c\tau}{(\omega_c\tau)^2 + (1 + j\omega\tau)^2}. \tag{5}$$

Here, ω is the frequency, τ is the scattering time, $\omega_c \approx eB_0 v_F^2/\mu_c$ is the cyclotron frequency, $v_F \approx 10^6 \mathrm{m} \cdot \mathrm{s}^{-1}$ is the Fermi velocity, e is the electron charge, μ_c is the chemical potential

$$\sigma_0 = \frac{e^2 \tau k_{\mathrm{B}} T}{\pi \hbar^2}\left[\frac{\mu_c}{k_{\mathrm{B}}T} + 2\ln\left(e^{-\mu_c/k_{\mathrm{B}}T} + 1\right)\right] \tag{6}$$

k_{B} is the Boltzmann's constant, $T = 300$ K is the temperature, and $\hbar$ is the reduced Planck's constant.

If the graphene sheet is not biased by a magnetic field, the surface conductivity $\overline{\overline{\sigma}}_{\mathrm{g}}$ reduces to a scalar and is expressed using the Kubo formula [38]: $\sigma_{\mathrm{g}} = \sigma_{\mathrm{intra}} + \sigma_{\mathrm{inter}}$. Here, the intraband and interband contributions σ_{intra} and σ_{inter} are given by

$$\sigma_{\mathrm{intra}} = \frac{2e^2}{\pi\hbar}\frac{k_{\mathrm{B}}T}{\hbar}\ln\left[2\cosh\left[\frac{\mu_c}{2k_BT}\right]\right]\frac{-\mathrm{j}}{\omega - \mathrm{j}\tau^{-1}} \tag{7}$$

$$\sigma_{\mathrm{inter}} = \frac{e^2}{4\hbar}\left(H\left(\frac{\omega}{2}\right) - \mathrm{j}\frac{4\omega}{\pi}\int_0^{\infty}\frac{H(\varepsilon) - H(\omega/2)}{\omega^2 - 4\varepsilon^2}\,d\varepsilon\right) \tag{8}$$

where function $H(\varepsilon)$ is defined as

$$H(\varepsilon) = \frac{\sinh(\hbar\varepsilon/k_{\mathrm{B}}T)}{\cosh(\mu_c/k_{\mathrm{B}}T) + \cosh(\hbar\varepsilon/k_{\mathrm{B}}T)}. \tag{9}$$

Note that in the rest of this section, the general case of a tensor-valued surface conductivity is assumed.

For traditional domain-decomposition formulations, RTCs are used to ensure the continuity of the electromagnetic fields on two sides of a surface that divides a domain into subdomains [39]. These traditional RTCs are given by Peng *et al.* [30]

$$\begin{aligned} \mathbf{J}_1 - \hat{\mathbf{n}}_1 \times \mathbf{M}_1 + \mathbf{J}_2 + \hat{\mathbf{n}}_2 \times \mathbf{M}_2 &= 0 \\ \hat{\mathbf{n}}_1 \times \mathbf{J}_1 + \mathbf{M}_1 - \hat{\mathbf{n}}_2 \times \mathbf{J}_2 + \mathbf{M}_2 &= 0. \end{aligned} \tag{10}$$

Here, $\mathbf{J}_1 = \hat{\mathbf{n}}_1 \times \mathbf{H}_1$, $\mathbf{J}_2 = \hat{\mathbf{n}}_2 \times \mathbf{H}_2$, $\mathbf{M}_1 = -\hat{\mathbf{n}}_1 \times \mathbf{E}_1$, $\mathbf{M}_2 = -\hat{\mathbf{n}}_2 \times \mathbf{E}_2$, and $\hat{\mathbf{n}}_2$ is the unit normal vector pointing into side 2.

Assume that the graphene sheet is located on a surface between two subdomains. Then, RTCs in (10) have to be modified to account for RBCs in (1) and (2). To derive these RRTCs, first, RBCs (1) and (2) are rewritten as

$$\mathbf{M}_1 + \mathbf{M}_2 = 0 \tag{11}$$

$$\mathbf{J}_1 + \mathbf{J}_2 - \overline{\overline{\sigma}}_{\mathrm{g}} \cdot \left(\hat{\mathbf{n}}_1 \times \mathbf{M}_1\right) = 0 \tag{12}$$

$$\mathbf{J}_1 + \mathbf{J}_2 - \overline{\overline{\sigma}}_{\mathrm{g}} \cdot \left(\hat{\mathbf{n}}_2 \times \mathbf{M}_2\right) = 0. \tag{13}$$

Then, linearly combining (11) and (12) as (12) $-$ $\hat{\mathbf{n}}_1$ $\times$ (11) and $\hat{\mathbf{n}}_1$ $\times$ (12) + (11) and using $\hat{\mathbf{n}}_1 = -\hat{\mathbf{n}}_2$ for $\mathbf{J}_2$ and $\mathbf{M}_2$ yield

$$\begin{aligned} \mathbf{J}_1 - \hat{\mathbf{n}}_1 \times \mathbf{M}_1 - \overline{\overline{\sigma}}_{\mathrm{g}} \cdot \left(\hat{\mathbf{n}}_1 \times \mathbf{M}_1\right) + \mathbf{J}_2 + \hat{\mathbf{n}}_2 \times \mathbf{M}_2 &= 0 \\ \hat{\mathbf{n}}_1 \times \mathbf{J}_1 + \mathbf{M}_1 + \overline{\overline{\sigma}}_{\mathrm{g}} \cdot \mathbf{M}_1 - \hat{\mathbf{n}}_2 \times \mathbf{J}_2 + \mathbf{M}_2 &= 0. \end{aligned} \tag{14}$$

This set of RRTCs is used when $\mathbf{r}$ approaches the surface from side 1. Linearly combining (11) and (13) as (13) $-$ $\hat{\mathbf{n}}_2$ $\times$ (11) and $\hat{\mathbf{n}}_2$ $\times$ (13) + (11) and using $\hat{\mathbf{n}}_2 = -\hat{\mathbf{n}}_1$ for $\mathbf{J}_1$ and $\mathbf{M}_1$ yield

$$\begin{aligned} \mathbf{J}_2 - \hat{\mathbf{n}}_2 \times \mathbf{M}_2 - \overline{\overline{\sigma}}_{\mathrm{g}} \cdot \left(\hat{\mathbf{n}}_2 \times \mathbf{M}_2\right) + \mathbf{J}_1 + \hat{\mathbf{n}}_1 \times \mathbf{M}_1 &= 0 \\ \hat{\mathbf{n}}_2 \times \mathbf{J}_2 + \mathbf{M}_2 + \overline{\overline{\sigma}}_{\mathrm{g}} \cdot \mathbf{M}_2 - \hat{\mathbf{n}}_1 \times \mathbf{J}_1 + \mathbf{M}_1 &= 0. \end{aligned} \tag{15}$$

This set of RRTCs is used when $\mathbf{r}$ approaches the surface from side 2. As expected, (14) and (15) are the same except that variables with subscripts 1 and 2 are interchanged. Also, note that (11)–(13) can be recovered by adding (14) to (15) and subtracting (14) from (15),

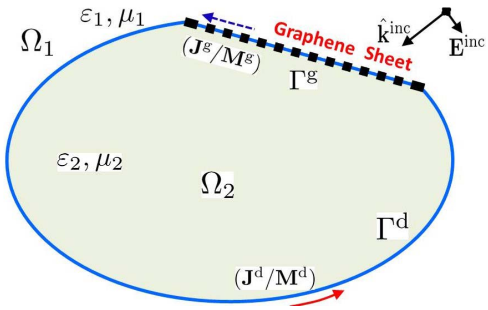

Fig. 1. Electromagnetic scattering from a graphene-based device.

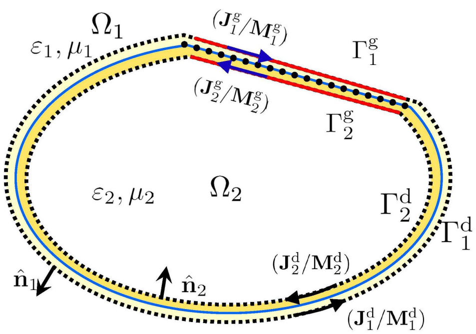

Fig. 2. Subdomains of the graphene-based device.

which also demonstrates that (14) and (15) are equivalent to (1) and (2) and they can be used to enforce these RBCs in the MT-SIE solver that is described in Section II-B.

B. MT-SIE Solver

The electromagnetic scattering scenario involving a graphene-based device is illustrated in Fig. 1. In this figure, $\boldsymbol{\Omega}_1$ and $\boldsymbol{\Omega}_2$ represent the dielectric substrate and the background medium, respectively. The graphene sheet is represented by Γ^{g} and is assumed to be located on the surface of the dielectric substrate. The part of the substrate surface, which is directly in touch with $\boldsymbol{\Omega}_1$ is represented by Γ^{d}. The permittivity, the permeability, the intrinsic impedance, and the wavenumber in $\boldsymbol{\Omega}_m$, $m \in \{1, 2\}$ are ε_m, μ_m, η_m, and k_m, respectively. The incident electromagnetic field, which originates in $\boldsymbol{\Omega}_1$, is represented by $\{\mathbf{E}_1^{\text{inc}}, \mathbf{H}_1^{\text{inc}}\}$.

The computation domain is naturally decomposed into two nonoverlapping subdomains as shown in Fig. 2: the exterior subdomain $\boldsymbol{\Omega}_1$ with boundary $\partial\boldsymbol{\Omega}_1$ and the inward-pointing unit normal vector $\hat{\mathbf{n}}_1$, and the interior dielectric subdomain $\boldsymbol{\Omega}_2$ with boundary $\partial\boldsymbol{\Omega}_2$ and the inward-pointing unit outward normal vector $\hat{\mathbf{n}}_2$. The surfaces that represent the graphene sheet and the dielectric substrate Γ^{g} and Γ^{d} have two sides/faces, each of which "touches" $\boldsymbol{\Omega}_1$ and $\boldsymbol{\Omega}_2$, that is, $\partial\boldsymbol{\Omega}_m = \Gamma_m^{\text{g}} \cup \Gamma_m^{\text{d}}$, $m \in \{1, 2\}$.

In each subdomain $\boldsymbol{\Omega}_m$, a boundary value problem (BVP) with Maxwell equations can be setup. This BVP is same as the one in [30], [32], and [33], but differently, RBCs have to be enforced on the graphene surface. The full set of boundary conditions enforced on $\partial\boldsymbol{\Omega}_m$ are expressed as

$$\pi_m^{\times}(\mathbf{H}_m) - \overline{\overline{\sigma}}_{\text{g}} \cdot \pi_m^{\tau}(\mathbf{E}_m) = -\pi_n^{\times}(\mathbf{H}_n) \text{ on } \Gamma_m^{\text{g}} \tag{16}$$

$$\pi_m^{\tau}(\mathbf{E}_m) = \pi_n^{\tau}(\mathbf{E}_n) \text{ on } \partial\boldsymbol{\Omega}_m = \Gamma_m^{\text{g}} \cup \Gamma_m^{\text{d}} \tag{17}$$

$$\pi_m^{\times}\left(\frac{1}{\mu_m}\nabla \times \mathbf{E}_m\right) = \pi_n^{\times}\left(\frac{1}{\mu_n}\nabla \times \mathbf{E}_n\right) \text{ on } n\ \Gamma_m^{\text{d}} \tag{18}$$

where $m, n \in \{1, 2\}, m \neq n$, $\{\mathbf{E}_m, \mathbf{H}_m\}$ are the electromagnetic fields in $\boldsymbol{\Omega}_m$, and the trace operators $\pi_m^{\tau}(\mathbf{u}) = \hat{\mathbf{n}}_m \times (\mathbf{u} \times \hat{\mathbf{n}}_m)|_{\partial\boldsymbol{\Omega}_m}$ and $\pi_m^{\times}(\mathbf{u}) = \hat{\mathbf{n}}_m \times \mathbf{u}|_{\partial\boldsymbol{\Omega}_m}$ represent tangential and twisted tangential components of $\mathbf{u}$ on $\partial\boldsymbol{\Omega}_m$, respectively. Electromagnetic fields in $\boldsymbol{\Omega}_m$ satisfy the fundamental field relations $\mathbf{E}_m = \mathbf{E}_m^{\text{sca}} + \mathbf{E}_m^{\text{inc}}$ and $\mathbf{H}_m = \mathbf{H}_m^{\text{sca}} + \mathbf{H}_m^{\text{inc}}$. Note that $\mathbf{E}_2^{\text{inc}}$ and $\mathbf{H}_2^{\text{inc}}$ are zero for the scattering problem considered here. Using Stratton-Chu representation, the scattered fields $\mathbf{E}_m^{\text{sca}}$ and $\mathbf{H}_m^{\text{sca}}$, $m \in \{1, 2\}$, are expressed as [40]

$$\begin{aligned}\mathbf{E}_m^{\text{sca}} &= \eta_m \mathcal{L}_m\{\mathbf{J}_m^{\text{d}}\} - \eta_0 \mathcal{K}_m\{\mathbf{M}_m^{\text{d}}\} + \eta_m \mathcal{L}_m\{\mathbf{J}_m^{\text{g}}\} \\ &\quad - \eta_0 \mathcal{K}_m\{\mathbf{M}_m^{\text{g}}\} \\ \eta_m \mathbf{H}_m^{\text{sca}} &= \eta_m \mathcal{K}_m\{\mathbf{J}_m^{\text{d}}\} + \eta_0 \mathcal{L}_m\{\mathbf{M}_m^{\text{d}}\} + \eta_m \mathcal{K}_m\{\mathbf{J}_m^{\text{g}}\} \\ &\quad + \eta_0 \mathcal{L}_m\{\mathbf{M}_m^{\text{g}}\}\end{aligned} \tag{19}$$

where η_0 is the intrinsic impedance in free space, $\mathbf{J}_m^{\text{d}} = \hat{\mathbf{n}}_m \times \mathbf{H}_{\Gamma_m^{\text{d}}}$ and $\mathbf{M}_m^{\text{d}} = -\hat{\mathbf{n}}_m \times \mathbf{E}_{\Gamma_m^{\text{d}}}$ and $\mathbf{J}_m^{\text{g}} = \hat{\mathbf{n}}_m \times \mathbf{H}_{\Gamma_m^{\text{g}}}$ and $\mathbf{M}_m^{\text{g}} = -\hat{\mathbf{n}}_m \times \mathbf{E}_{\Gamma_m^{\text{g}}}$ are the (unknown) equivalent electric and magnetic currents introduced on Γ_m^{d} and Γ_m^{g}, respectively. In (19), operators $\mathcal{L}_m$ and $\mathcal{K}_m$ are given by Zhao *et al.* [32], [33]

$$\mathcal{L}_m\{\mathbf{X}_m^{\text{e}}\}(\mathbf{r}) = -jk_m \int_{\Gamma_m^{\text{e}}} \left[\mathbf{I} + \frac{1}{k_m^2}\nabla\nabla\cdot\right] \mathbf{X}_m^{\text{e}}(\mathbf{r}') G_m(\mathbf{r}, \mathbf{r}')\, ds'$$

$$\mathcal{K}_m\{\mathbf{X}_m^{\text{e}}\}(\mathbf{r}) = \int_{\Gamma_m^{\text{e}}} \nabla G_m(\mathbf{r}, \mathbf{r}') \times \mathbf{X}_m^{\text{e}}(\mathbf{r}')\, ds'$$

where $\text{e} \in \{\text{d}, \text{g}\}$ and G_m is the Green function of the unbounded medium with wavenumber k_m. Note that $\mathcal{K}_m\{\mathbf{X}_m^{\text{e}}\} = \hat{\mathbf{n}}_m \times \mathbf{X}_m^{\text{e}}/2 + \overline{\mathcal{K}}_m\{\mathbf{X}_m^{\text{e}}\}$, where $\overline{\mathcal{K}}_m$ is the principal value of $\mathcal{K}_m$. Inserting (19) into the tangential components of the fundamental field relations on Γ_m^{d} and Γ_m^{g} yield $\mathbf{E}$- and $\mathbf{H}$-field equations in $\boldsymbol{\Omega}_m$ as [28]

$$\begin{aligned}&\frac{\eta_0}{2}\pi_m^{\times}(\mathbf{M}_m^{\text{d}}) + \eta_0 \pi_m^{\tau}\left(\overline{\mathcal{K}}_m\{\mathbf{M}_m^{\text{d}}\} + \mathcal{K}_m\{\mathbf{M}_m^{\text{g}}\}\right) \\ &\quad - \eta_m \pi_m^{\tau}\left(\mathcal{L}_m\{\mathbf{J}_m^{\text{d}}\} + \mathcal{L}_m\{\mathbf{J}_m^{\text{g}}\}\right) = \pi_m^{\tau}(\mathbf{E}^{\text{inc}}) \text{ on } \Gamma_m^{\text{d}} \\ &-\frac{\eta_0}{2}\pi_m^{\times}(\mathbf{J}_m^{\text{d}}) - \eta_0 \pi_m^{\tau}\left(\mathcal{K}_m\{\mathbf{J}_m^{\text{d}}\} + \overline{\mathcal{K}}_m\{\mathbf{J}_m^{\text{g}}\}\right) \\ &\quad - \frac{\eta_0}{\eta_m}\pi_m^{\tau}\left(\mathcal{L}_m\{\mathbf{M}_m^{\text{d}}\} + \mathcal{L}_m\{\mathbf{M}_m^{\text{g}}\}\right) = \eta_0 \pi_m^{\tau}(\mathbf{H}^{\text{inc}}) \text{ on } \Gamma_m^{\text{d}}\end{aligned} \tag{20}$$

$$\begin{aligned}&\frac{\eta_0}{2}\pi_m^{\times}(\mathbf{M}_m^{\text{g}}) + \eta_0 \pi_m^{\tau}\left(\mathcal{K}_m\{\mathbf{M}_m^{\text{d}}\} + \overline{\mathcal{K}}_m\{\mathbf{M}_m^{\text{g}}\}\right) \\ &\quad - \eta_m \pi_m^{\tau}\left(\mathcal{L}_m\{\mathbf{J}_m^{\text{d}}\} + \mathcal{L}_m\{\mathbf{J}_m^{\text{g}}\}\right) = \pi_m^{\tau}(\mathbf{E}^{\text{inc}}) \text{ on } \Gamma_m^{\text{g}} \\ &-\frac{\eta_0}{2}\pi_m^{\times}(\mathbf{J}_m^{\text{g}}) - \eta_0 \pi_m^{\tau}\left(\mathcal{K}_m\{\mathbf{J}_m^{\text{d}}\} + \overline{\mathcal{K}}_m\{\mathbf{J}_m^{\text{g}}\}\right) \\ &\quad - \frac{\eta_0}{\eta_m}\pi_m^{\tau}\left(\mathcal{L}_m\{\mathbf{M}_m^{\text{d}}\} + \mathcal{L}_m\{\mathbf{M}_m^{\text{g}}\}\right) = \eta_0 \pi_m^{\tau}(\mathbf{H}^{\text{inc}}) \text{ on } \Gamma_m^{\text{g}}.\end{aligned} \tag{21}$$

To enforce the boundary conditions (16)–(18), (20) and (10) are combined on Γ_m^{d} and (21) and (14) are combined on Γ_m^{g}, leading to

$$\begin{aligned}&\frac{\eta_0}{2}\mathbf{J}_m^{\text{d}} - \eta_0 \eta_m \pi_m^{\tau}\left(\mathcal{L}_m\{\mathbf{J}_m^{\text{d}}\} + \mathcal{L}_m\{\mathbf{J}_m^{\text{g}}\}\right) \\ &\quad - \eta_0 \pi_m^{\tau}\left(\overline{\mathcal{K}}_m\{\mathbf{M}_m^{\text{d}}\} + \mathcal{K}_m\{\mathbf{M}_m^{\text{g}}\}\right) \\ &\quad + \frac{\eta_0}{2}\mathbf{J}_n^{\text{d}} + \frac{\eta_0}{2}\pi_n^{\times}(\mathbf{M}_n^{\text{d}}) = \pi_m^{\tau}(\mathbf{E}^{\text{inc}}) \text{ on } \Gamma_m^{\text{d}} \\ &\frac{\eta_0}{2}\mathbf{M}_m^{\text{d}} - \frac{\eta_0}{\eta_m}\pi_m^{\tau}\left(\mathcal{L}_m\{\mathbf{M}_m^{\text{d}}\} + \mathcal{L}_m\{\mathbf{M}_m^{\text{g}}\}\right) \\ &\quad - \eta_0 \pi_m^{\tau}\left(\overline{\mathcal{K}}_m\{\mathbf{J}_m^{\text{d}}\} + \mathcal{K}_m\{\mathbf{J}_m^{\text{g}}\}\right) \\ &\quad + \frac{\eta_0}{2}\mathbf{M}_n^{\text{d}} - \frac{\eta_0}{2}\pi_n^{\times}(\mathbf{J}_n^{\text{d}}) = \eta_0 \pi_m^{\tau}(\mathbf{H}^{\text{inc}}) \text{ on } \Gamma_m^{\text{d}} \\ &\frac{\eta_0}{2}\mathbf{J}_m^{\text{g}} - \frac{\eta_0}{2}\overline{\overline{\sigma}}_{\text{g}} \cdot \pi_m^{\times}(\mathbf{M}_m^{\text{g}}) - \eta_0 \eta_m \pi_m^{\tau}\left(\mathcal{L}_m\{\mathbf{J}_m^{\text{d}}\} + \mathcal{L}_m\{\mathbf{J}_m^{\text{g}}\}\right) \\ &\quad + \eta_0 \pi_m^{\tau}\left(\mathcal{K}_m\{\mathbf{M}_m^{\text{d}}\} + \overline{\mathcal{K}}_m\{\mathbf{M}_m^{\text{g}}\}\right) \\ &\quad + \frac{\eta_0}{2}\mathbf{J}_n^{\text{g}} + \frac{\eta_0}{2}\pi_n^{\times}(\mathbf{M}_n^{\text{g}}) = \pi_m^{\tau}(\mathbf{E}^{\text{inc}}) \text{ on } \Gamma_m^{\text{g}} \\ &\frac{\eta_0}{2}\mathbf{M}_m^{\text{g}} + \frac{\eta_0}{2}\overline{\overline{\sigma}}_{\text{g}} \cdot \mathbf{M}_m^{\text{g}} - \frac{\eta_0}{\eta_m}\pi_m^{\tau}\left(\mathcal{L}_m\{\mathbf{M}_m^{\text{d}}\}\right.\end{aligned} \tag{22}$$

$$+\mathcal{L}_m\{\mathbf{M}_m^{\mathrm{g}}\}) - \eta_0\pi_m^{\tau}(\mathcal{K}_m\{\mathbf{J}_m^{\mathrm{d}}\} + \overline{\mathcal{K}}_m\{\mathbf{J}_m^{\mathrm{g}}\})$$
$$+\frac{\eta_0}{2}\mathbf{M}_n^{\mathrm{g}} - \frac{\eta_0}{2}\pi_n^{\times}(\mathbf{J}_n^{\mathrm{g}}) = \eta_0\pi_m^{\tau}(\mathbf{H}^{\mathrm{inc}}) \text{ on } \Gamma_m^{\mathrm{g}}. \quad (23)$$

To numerically solve (22) and (23), first Γ^{d} and Γ^{g} are discretized into a mesh of triangular patches. Then, the unknown electric and magnetic currents on Γ_m^{d} and Γ_m^{g}, $m \in \{1, 2\}$, are expanded using RWG basis function sets $\mathbf{j}_m$ and $\mathbf{m}_m$, respectively [29]. Inserting these expansions into (22) and (23) and applying the Galerkin testing to the resulting equations yield a linear matrix system

$$\begin{bmatrix} \mathbf{A}_1 & \mathbf{M}_{12} \\ \mathbf{M}_{21} & \mathbf{A}_2 \end{bmatrix} \begin{bmatrix} \mathbf{I}_1 \\ \mathbf{I}_2 \end{bmatrix} = \begin{bmatrix} \mathbf{V}_0 \\ \mathbf{0} \end{bmatrix} \quad (24)$$

where matrices $\mathbf{A}_m$ and $\mathbf{M}_{mn}$, $m, n \in \{1, 2\}$, $n \neq m$, represent the "self" and "coupled" electromagnetic interactions in $\mathbf{\Omega}_m$ and between $\mathbf{\Omega}_m$ and $\mathbf{\Omega}_n$, respectively. Vectors $\mathbf{I}_m$ store the unknown coefficients of basis function sets $\mathbf{j}_m$ and $\mathbf{m}_m$ and $\mathbf{V}_0$ stores the tested incident fields. $\mathbf{A}_m$ are dense matrices and expressed as

$$\mathbf{A}_m = \begin{bmatrix} \mathbf{A}_m^{\mathrm{JJ}} & \mathbf{A}_m^{\mathrm{JM}} \\ \mathbf{A}_m^{\mathrm{MJ}} & \mathbf{A}_m^{\mathrm{MM}} \end{bmatrix} \quad (25)$$

where the each matrix block is given by

$$\begin{aligned}
\mathbf{A}_m^{\mathrm{JJ}} &= \left\langle \mathbf{j}_m, \frac{\eta_0}{2}\mathbf{j}_m - \eta_n\pi_m^{\tau}(\mathcal{L}_m\{\mathbf{j}_m\})\right\rangle_{\partial\Omega_m} \\
\mathbf{A}_m^{\mathrm{JM}} &= \langle \mathbf{j}_m, \eta_0\pi_m^{\tau}(\overline{\mathcal{K}}_m\{\mathbf{m}_m\})\rangle_{\partial\Omega_m} \\
&\quad - \left\langle \mathbf{j}_m, \frac{\eta_0}{2}\overline{\overline{\sigma}}_{\mathrm{g}} \cdot \pi_m^{\times}(\mathbf{m}_m)\right\rangle_{\Gamma_m^{\mathrm{g}}} \\
\mathbf{A}_m^{\mathrm{MJ}} &= \langle \mathbf{m}_m, -\eta_0\pi_m^{\tau}(\overline{\mathcal{K}}_m\{\mathbf{j}_m\})\rangle_{\partial\Omega_m} \\
\mathbf{A}_m^{\mathrm{MM}} &= \left\langle \mathbf{m}_m, \frac{\eta_0}{2}\mathbf{m}_m - \frac{1}{\eta_m}\pi_m^{\tau}(\mathcal{L}_m\{\mathbf{m}_m\})\right\rangle_{\partial\Omega_m} \\
&\quad + \left\langle \mathbf{m}_m, \frac{\eta_0}{2}\overline{\overline{\sigma}}_{\mathrm{g}} \cdot \mathbf{m}_m\right\rangle_{\Gamma_m^{\mathrm{g}}}.
\end{aligned} \quad (26)$$

Here, $\rangle\mathbf{u}, \mathbf{v}\langle$ denotes the inner product of two complex vector functions $\mathbf{u}$ and $\mathbf{v}$

$$\langle \mathbf{u}, \mathbf{v}\rangle_{\Gamma} = \int_{\Gamma} (\mathbf{u} \cdot \mathbf{v})\, d\Gamma. \quad (27)$$

Since the coupling between electromagnetic fields in two subdomains is accounted for using RTCs and RRTCs, matrices $\mathbf{M}_{mn}$ are sparse. They are expressed as

$$\mathbf{M}_{mn} = \begin{bmatrix} \frac{\eta_m}{2}\langle \mathbf{j}_m, \mathbf{j}_n\rangle_{\partial\Omega_m} & \frac{\eta_0}{2}\langle \mathbf{j}_m, \pi_n^{\times}(\mathbf{m}_n)\rangle_{\partial\Omega_m} \\ \frac{\eta_0}{2}\langle \mathbf{m}_m, \pi_n^{\times}(\mathbf{j}_n)\rangle_{\partial\Omega_m} & -\frac{\eta_m}{2}\langle \mathbf{m}_m, \mathbf{m}_n\rangle_{\partial\Omega_m} \end{bmatrix}. \quad (28)$$

In (25), the right-hand side vector $\mathbf{V}_0 = [\mathbf{V}_0^{\mathrm{J}}\, \mathbf{V}_0^{\mathrm{M}}]^T$, where

$$\begin{aligned}
\mathbf{V}_0^{\mathrm{J}} &= \left\langle \mathbf{j}_0, \pi_m^{\tau}(\mathbf{E}^{\mathrm{inc}})\right\rangle_{\partial\Omega_0} \\
\mathbf{V}_m^{\mathrm{M}} &= \left\langle \mathbf{m}_0, \eta_0\pi_m^{\tau}(\mathbf{H}^{\mathrm{inc}})\right\rangle_{\partial\Omega_0}.
\end{aligned} \quad (29)$$

The matrix system (24) is solved iteratively using the generalized minimal residual method scheme (GMRES) [41]. The computational cost of multiplying $\mathbf{A}_1$ and $\mathbf{A}_2$ by vectors scales as $O(N^2)$. While using the multilevel fast multipole algorithm (MLFMA), the cost is reduced to $O(N\log N)$ [42], [43]. The computational cost of multiplying sparse matrices $\mathbf{M}_{12}$ and $\mathbf{M}_{21}$ by vectors is $O(N)$.

III. Numerical Results

In this section, several numerical examples, which demonstrate the accuracy and the applicability of the proposed MT-SIE solver, are presented. In all examples, it is assumed that the background medium $\mathbf{\Omega}_1$ is free space with permittivity ε_0 and permeability μ_0, and the excitation is a plane wave with electric field $\mathbf{E}^{\mathrm{inc}}(\mathbf{r}) = E_0\hat{\mathbf{p}}e^{-jk_0\hat{\mathbf{k}}\cdot\mathbf{r}}$. Here, $E_0 = 1$ V/m is the amplitude, $\hat{\mathbf{p}}$ is the polarization vector, $\hat{\mathbf{k}}$ is the direction of propagation, and $k_0 = 2\pi/\lambda_0$ and λ_0 are the wavenumber and the wavelength in free space, respectively. The substrates are nonmagnetic with permeability μ_0. For all examples considered in this section, the GMRES iterations are terminated when the relative residual reaches 0.001.

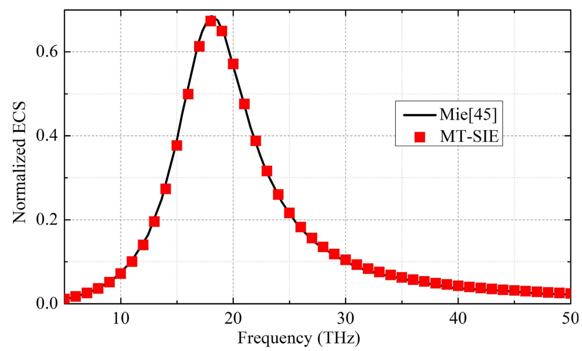

Fig. 3. Normalized ECS of the spherical graphene surface.

A. Nonmagnetized Spherical Graphene Surface

In the first example, scattering from a spherical graphene surface is investigated. The surface is centered at the origin, its radius is 200 nm, and the permittivity and the permeability inside the surface are ε_0 and μ_0, respectively. The parameters of the graphene are $\mu_c = 0.3$ eV and $\tau = 0.02$ ps. The excitation parameters are $\hat{\mathbf{p}} = \hat{\mathbf{x}}$ and $\hat{\mathbf{k}} = -\hat{\mathbf{z}}$, and the frequency is swept from 0.5 to 50 THz. The spherical surface is discretized using 532 triangular patches, which corresponds to an average edge length of 45 nm ($\lambda_0/133$ at 50 THz).

First, the equivalent electric and magnetic currents on the inner and outer surfaces of the sphere are computed by solving (24). Then, the currents on the outer surface are used to compute the extinction cross section (ECS) [44], [45]. Fig. 3 compares this ECS (which is normalized by the sphere's geometrical cross section) to ECS computed using the analytical solution [46]. The results agree very well, which demonstrates the accuracy of the proposed MT-SIE solver.

B. Magnetized Graphene Patch

In this example, scattering from a magnetized graphene patch of dimensions 10 μm×2 μm (along x- and y-directions, respectively) is investigated. It is assumed that the patch is centered on the top surface of a substrate with dimensions 10 μm×2 μm×0.15 μm (along x-, y-, and z-directions, respectively). The permittivity of the substrate is ε_0. This ensures that the structure simulated by the MT-SIE solver is equivalent to a magnetized graphene patch that resides in free space. The parameters of the graphene are $\tau = 0.33$ ps, $B_0 = 0.25$ T, and $\mu_c \in \{0.5, 1.0, 1.5\}$ eV. The excitation parameters are $\hat{\mathbf{p}} = \hat{\mathbf{x}}$ and $\hat{\mathbf{k}} = -\hat{\mathbf{z}}$, and the frequency is swept from 0.1 to 10 THz. The surfaces of the patch and the substrate are discretized into 474 and 632 triangular patches, respectively, which corresponds to an average edge length of 0.3 μm ($\lambda_0/100$ at 10 THz).

Fig. 4 plots the absorption cross section (ACS) [44], [45] obtained using the equivalent currents computed by the MT-SIE solver for three different values of μ_c and compares it to ACS provided in [19] and [21]. Results agree well.

C. Magnetized Graphene Patch on a Dielectric Substrate

Next, scattering from a magnetized graphene patch of dimensions 150 μm × 150 μm (along x- and y-directions, respectively), which

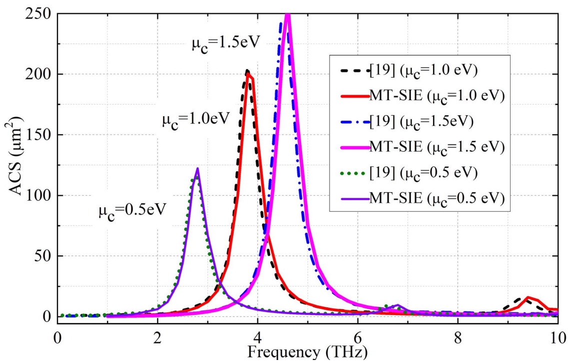

Fig. 4. ACS of the magnetized graphene sheet for $\mu_c \in \{0.5, 1.0, 1.5\}$ eV.

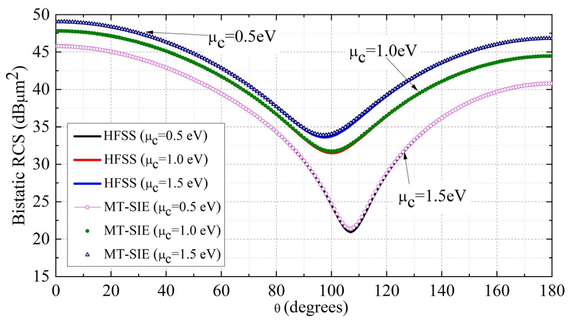

Fig. 5. Bistatic RCS of the magnetized graphene sheet on a dielectric substrate for $\mu_c \in \{0.5, 1.0, 1.5\}$ eV.

is centered on the top surface of a dielectric substrate of dimensions 150 μm $\times$ 150 μm $\times$ 30 μm (along x-, y-, and z-directions, respectively) is investigated. The permittivity of the substrate is $4.0\varepsilon_0$. The parameters of the graphene and the excitation are the same as those in the previous example. The frequency is 1 THz. The surfaces of the patch and the substrate are discretized into 208 and 584 triangular patches, respectively, which corresponds to an average edge length of 15 μm ($\lambda_0/20$ at 1 THz).

Fig. 5 plots the copolarized bistatic radar cross section (RCS) (on the $\phi = 0$ plane) obtained using the equivalent currents computed by the MT-SIE solver for $\mu_c \in \{0.5, 1.0, 1.5\}$ eV and compares it to RCS obtained using the finite-element method-based commercial software HFSS. Results agree well and also show that RCS decreases with increasing μ_c. For this example, GMRES (without a preconditioner) requires 153, 175, and 189 iterations for simulations with $\mu_c = 0.5$, 1.0, and 1.5 eV, respectively.

D. THz Polarization Converter

In this example, scattering from a tunable THz reflective linear polarization converter is analyzed [47]. The geometry and the dimensions of the structure are shown in Fig. 6. The permittivity of the substrate is $2.2\varepsilon_0$. The parameters of the graphene are $\mu_c = 0.5$ eV and $\tau = 1.0$ ps and the excitation parameters are $\hat{\mathbf{p}} = \hat{\mathbf{x}}$ and $\hat{\mathbf{k}} = -\hat{\mathbf{z}}$. The frequency is 1 THz. The surfaces of the 49 oval-shaped patches and the substrate are discretized using 3871 and 3709 triangular patches, respectively, which corresponds to an average edge length of 13 μm ($\lambda_0/25$ at 1 THz).

Fig. 7 plots the copolarized and cross-polarized bistatic RCS (on $\phi = 0$ plane) obtained using the equivalent currents computed by the MT-SIE solver and compares it to RCS obtained using HFSS. Results agree well. The figure also shows that the cross-polarized reflection is enhanced by the polarization converter. Table I compares the computational requirements of the MT-SIE solver (without a preconditioner

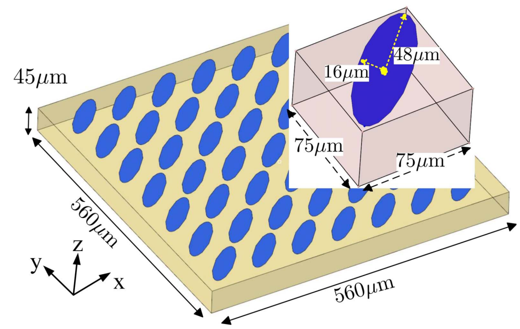

Fig. 6. Geometry and the dimensions of the THz polarization converter.

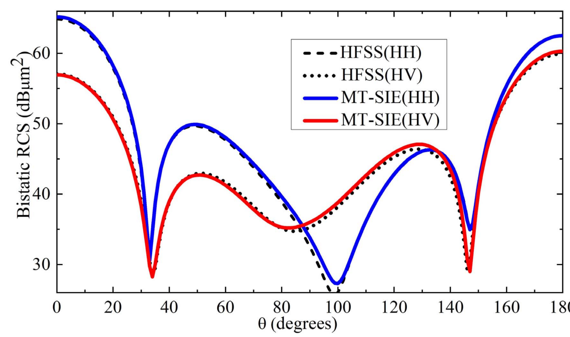

Fig. 7. Copolarized and cross-polarized RCS of the THz polarization converter.

TABLE I
COMPUTATIONAL REQUIREMENTS FOR SIMULATIONS OF THE THz POLARIZATION CONVERTER

	Time	Memory	Iterations
MT-SIE (SAI preconditioner)	30 m	2.99 GB	30
MT-SIE (no preconditioner)	10 m	1.58 GB	399
HFSS	1 h 54 m	42.1 GB	N/A

and with the sparse-approximate-inverse (SAI) preconditioner [48]) to those of HFSS and clearly shows that the MT-SIE solver is faster and uses significantly less memory.

IV. CONCLUSION

An MT-SIE solver is formulated and implemented to analyze electromagnetic field interactions on composite devices involving graphene sheets. This solver decomposes the computation domain into exterior and interior subdomains, which represent the unbounded background medium and the dielectric substrate, respectively. The electric and magnetic field equations are used as the governing equations in each subdomain. RRTCs are derived for the first time to account for the infinitesimally thin graphene sheet that is located on the interface between these two subdomains. The governing equations of a subdomain are locally coupled to the governing equations of its neighbor using RRTCs and RTCs. The accuracy and the applicability of the MT-SIE solver are demonstrated by various numerical examples.

REFERENCES

[1] A. K. Geim and K. S. Novoselov, "The rise of graphene," *Nature Mater.*, vol. 6, no. 3, pp. 183–191, 2007.
[2] W.-Z. Xu *et al.*, "Electrically tunable terahertz metamaterials with embedded large-area transparent thin-film transistor arrays," *Sci. Rep.*, vol. 6, no. 1, pp. 1–9, Sep. 2016.

[3] A. Lipatov, A. Varezhnikov, P. Wilson, V. Sysoev, A. Kolmakov, and A. Sinitskii, "Highly selective gas sensor arrays based on thermally reduced graphene oxide," *Nanoscale*, vol. 5, no. 12, pp. 5426–5434, Jun. 2013.

[4] F. Vaianella, G. Rosolen, and B. Maes, "Graphene as a transparent electrode for amorphous silicon-based solar cells," *J. Appl. Phys.*, vol. 117, no. 24, 2015, Art. no. 243102.

[5] J. Gosciniak and D. T. H. Tan, "Theoretical investigation of graphene-based photonic modulators," *Sci. Rep.*, vol. 3, no. 1, pp. 1–6, Dec. 2013.

[6] D. Correas-Serrano, J. S. Gómez-Díaz, J. Perruisseau-Carrier, and A. Alvarez-Melcon, "Graphene-based plasmonic tunable low-pass filters in the terahertz band," *IEEE Trans. Nanotechnol.*, vol. 13, no. 6, pp. 1145–1153, Nov. 2014.

[7] P. Y. Chen, C. Argyropoulos, and A. Alù, "Terahertz antenna phase shifters using integrally-gated graphene transmission-lines," *IEEE Trans. Antennas Propag.*, vol. 61, no. 4, pp. 1528–1537, Apr. 2012.

[8] M. Esquius-Morote, J. S. Gómez-Díaz, and J. Perruisseau-Carrier, "Sinusoidally modulated graphene leaky-wave antenna for electronic beamscanning at THz," *IEEE Trans. THz Sci. Technol.*, vol. 4, no. 1, pp. 116–122, Jan. 2014.

[9] D. Correas-Serrano and J. S. Gómez-Díaz, "Graphene-based antennas for terahertz systems: A review," 2017, *arXiv:1704.00371*. [Online]. Available: https://arxiv.org/abs/1704.00371

[10] X. Li, L. Lin, L.-S. Wu, W.-Y. Yin, and J.-F. Mao, "A bandpass graphene frequency selective surface with tunable polarization rotation for THz applications," *IEEE Trans. Antennas Propag.*, vol. 65, no. 2, pp. 662–672, Feb. 2016.

[11] J. Chen, G. Hao, and Q.-H. Liu, "Using the ADI-FDTD method to simulate graphene-based FSS at terahertz frequency," *IEEE Trans. Electromagn. Compat.*, vol. 59, no. 4, pp. 1218–1223, Aug. 2017.

[12] I. Ahmed, E. H. Khoo, and E. Li, "Efficient modeling and simulation of graphene devices with the LOD-FDTD method," *IEEE Microw. Wireless Compon. Lett.*, vol. 23, no. 6, pp. 306–308, Jun. 2013.

[13] X.-H. Wang, W.-Y. Yin, and Z. Chen, "Matrix exponential FDTD modeling of magnetized graphene sheet," *IEEE Antennas Wireless Propag. Lett.*, vol. 12, pp. 1129–1132, 2013.

[14] V. Nayyeri, M. Soleimani, and O. M. Ramahi, "Wideband modeling of graphene using the finite-difference time-domain method," *IEEE Trans. Antennas Propag.*, vol. 61, no. 12, pp. 6107–6114, Dec. 2013.

[15] V. Nayyeri, M. Soleimani, and O. M. Ramahi, "Modeling graphene in the finite-difference time-domain method using a surface boundary condition," *IEEE Trans. Antennas Propag.*, vol. 61, no. 8, pp. 4176–4182, Aug. 2013.

[16] P. Li, L. J. Jiang, and H. Bagci, "A resistive boundary condition enhanced DGTD scheme for the transient analysis of graphene," *IEEE Trans. Antennas Propag.*, vol. 63, no. 7, pp. 3065–3076, Jul. 2015.

[17] P. Wang, Y. Shi, C.-Y. Tian, and L. Li, "Analysis of graphene-based devices using wave equation based discontinuous Galerkin time-domain method," *IEEE Antennas Wireless Propag. Lett.*, vol. 17, no. 12, pp. 2169–2173, Dec. 2018.

[18] Y. Zhao, S. Tao, D. Ding, and R. Chen, "A time-domain thin dielectric sheet (TD-TDS) integral equation method for scattering characteristics of tunable graphene," *IEEE Trans. Antennas Propag.*, vol. 66, no. 3, pp. 1366–1373, Mar. 2018.

[19] L. Guan, S. Tao, Y. Zhao, and R. Chen, "An anisotropic thin dielectric sheet method for analysis of magnetized graphene," *IEEE Antennas Wireless Propag. Lett.*, vol. 18, no. 2, pp. 279–282, Feb. 2018.

[20] I.-T. Chiang and W. C. Chew, "Thin dielectric sheet simulation by surface integral equation using modified RWG and pulse bases," *IEEE Trans. Antennas Propag.*, vol. 54, no. 7, pp. 1927–1934, Jul. 2006.

[21] Y. S. Cao, L. J. Jiang, and A. E. Ruehli, "An equivalent circuit model for graphene-based terahertz antenna using the PEEC method," *IEEE Trans. Antennas Propag.*, vol. 64, no. 4, pp. 1385–1393, Apr. 2016.

[22] Y. S. Cao, P. Li, L. J. Jiang, and A. E. Ruehli, "The derived equivalent circuit model for magnetized anisotropic graphene," *IEEE Trans. Antennas Propag.*, vol. 65, no. 2, pp. 948–953, Feb. 2016.

[23] A. E. Ruehli, "Equivalent circuit models for three-dimensional multiconductor systems," *IEEE Trans. Microw. Theory Techn.*, vol. MTT-22, no. 3, pp. 216–221, Mar. 1974.

[24] O. V. Shapoval, J. S. Gómez-Díaz, J. Perruisseau-Carrier, J. R. Mosig, and A. I. Nosich, "Integral equation analysis of plane wave scattering by coplanar graphene-strip gratings in the THz range," *IEEE Trans. THz Sci. Technol.*, vol. 3, no. 5, pp. 666–674, Sep. 2013.

[25] M. V. Balaban, O. V. Shapoval, and A. I. Nosich, "THz wave scattering by a graphene strip and a disk in the free space: Integral equation analysis and surface plasmon resonances," *J. Opt.*, vol. 15, no. 11, Nov. 2013, Art. no. 114007.

[26] Y. Shi, P. Li, I. E. Uysal, H. A. Ulku, and H. Bagci, "An MOT-TDIE solver for analyzing transient fields on graphene-based devices," in *Proc. IEEE Int. Symp. Antennas Propag. (APSURSI)*, Jun. 2016, pp. 2093–2094.

[27] L. L. Meng, T. Xia, X. Y. Xiong, L. J. Jiang, and W. C. Chew, "Analysis of nonlinear graphene plasmonics using surface integral equations," in *Proc. Appl. Comput. Electromagn. Symp.*, 2018, pp. 1–2.

[28] Y. Chang and R. F. Harrington, "A surface formulation for characteristic modes of material bodies," *IEEE Trans. Antennas Propag.*, vol. AP-25, no. 6, pp. 789–795, Nov. 1977.

[29] S. M. Rao, D. R. Wilton, and A. W. Glisson, "Electromagnetic scattering by surfaces of arbitrary shape," *IEEE Trans. Antennas Propag.*, vol. AP-30, no. 3, pp. 409–418, May 1982.

[30] Z. Peng, K.-H. Lim, and J.-F. Lee, "Computations of electromagnetic wave scattering from penetrable composite targets using a surface integral equation method with multiple traces," *IEEE Trans. Antennas Propag.*, vol. 61, no. 1, pp. 256–270, Jan. 2012.

[31] Z. Peng, "A novel multitrace boundary integral equation formulation for electromagnetic cavity scattering problems," *IEEE Trans. Antennas Propag.*, vol. 63, no. 10, pp. 4446–4457, Oct. 2015.

[32] R. Zhao, Z. Huang, W.-F. Huang, J. Hu, and X. Wu, "Multiple-traces surface integral equations for electromagnetic scattering from complex microstrip structures," *IEEE Trans. Antennas Propag.*, vol. 66, no. 7, pp. 3804–3809, Jul. 2018.

[33] R. Zhao, Y. Chen, X.-M. Gu, Z. Huang, H. Bagci, and J. Hu, "A local coupling multitrace domain decomposition method for electromagnetic scattering from multilayered dielectric objects," *IEEE Trans. Antennas Propag.*, vol. 68, no. 10, pp. 7099–7108, Oct. 2020.

[34] R. Zhao, P. Li, J. Hu, and H. Bagci, "A multitrace surface integral equation method for PEC/dielectric composite objects," *IEEE Antennas Wireless Propag. Lett.*, vol. 20, no. 8, pp. 1404–1408, Aug. 2021.

[35] K. Achouri, M. A. Salem, and C. Caloz, "General metasurface synthesis based on susceptibility tensors," *IEEE Trans. Antennas Propag.*, vol. 63, no. 7, pp. 2977–2991, Jul. 2015.

[36] X. Du, H. Yu, and M. Li, "Effective modeling of tunable graphene with dispersive FDTD-GSTC method," *Appl. Comput. Electromagn. Soc. J.*, vol. 31, no. 6, pp. 851–857, 2019.

[37] G. W. Hanson, "Dyadic Green's functions for an anisotropic, non-local model of biased graphene," *IEEE Trans. Antennas Propag.*, vol. 56, no. 3, pp. 747–757, Mar. 2008.

[38] G. W. Hanson, "Dyadic Green's functions and guided surface waves for a surface conductivity model of graphene," *J. Appl. Phys.*, vol. 103, no. 6, Mar. 2008, Art. no. 064302.

[39] Z. Peng, X.-C. Wang, and J.-F. Lee, "Integral equation based domain decomposition method for solving electromagnetic wave scattering from non-penetrable objects," *IEEE Trans. Antennas Propag.*, vol. 59, no. 9, pp. 3328–3338, Sep. 2011.

[40] C. A. Balanis, *Advanced Engineering Electromagnetics*. Hoboken, NJ, USA: Wiley, 2012.

[41] Y. Saad and M. H. Schultz, "GMRES: A generalized minimal residual algorithm for solving nonsymmetric linear systems," *SIAM J. Sci. Statist. Comput.*, vol. 7, no. 3, pp. 856–869, 1986.

[42] J. M. Song, C.-C. Lu, and W. C. Chew, "Multilevel fast multipole algorithm for electromagnetic scattering by large complex objects," *IEEE Trans. Antennas Propag.*, vol. 45, no. 10, pp. 1488–1493, Oct. 1997.

[43] A. C. Yucel, W. Sheng, C. Zhou, Y. Liu, H. Bagci, and E. Michielssen, "An FMM-FFT accelerated SIE simulator for analyzing EM wave propagation in mine environments loaded with conductors," *IEEE J. Multiscale Multiphys. Comput. Tech.*, vol. 3, pp. 3–15, 2018.

[44] M. I. Mishchenko, L. D. Travis, and A. A. Lacis, *Scattering, Absorption, Amission Light by Small Particles*. Cambridge, U.K.: Cambridge Univ. Press, 2002.

[45] I. E. Uysal, H. A. Ülkü, and H. Bağci, "Transient analysis of electromagnetic wave interactions on plasmonic nanostructures using a surface integral equation solver," *J. Opt. Soc. Amer. A, Opt. Image Sci.*, vol. 33, no. 9, pp. 1747–1759, 2016.

[46] S. H. Raad, Z. Atlasbaf, J. Rashed-Mohassel, and M. Shahabadi, "Scattering from graphene-based multilayered spherical structures," *IEEE Trans. Nanotechnol.*, vol. 18, pp. 1129–1136, 2019.

[47] H. Zhang and Y. Cheng, "Tunable terahertz reflective linear polarization convertor based on oval-shape-perforated graphene metasurface," in *Proc. Asia Commun. Photon. Conf. (ACP)*, Oct. 2018, p. Su2A.265.

[48] J. Lee, J. Zhang, and C.-C. Lu, "Sparse inverse preconditioning of multilevel fast multipole algorithm for hybrid integral equations in electromagnetics," *IEEE Trans. Antennas Propag.*, vol. 52, no. 9, pp. 2277–2287, Sep. 2004.